

Highly Tunable Two-Qubit Interactions in Si/SiGe Quantum Dots by Interchanging the Roles of Qubit-Defining Gates

Jaemin Park¹, Hyeongyu Jang¹, Hanseo Sohn¹, Younguk Song¹, Lucas E. A. Stehouwer²,
Davide Degli Esposti², Giordano Scappucci², and Dohun Kim^{1*}

¹*NextQuantum, Department of Physics and Astronomy, and Institute of Applied Physics, Seoul National University, Seoul 08826, Korea*

²*QuTech and Kavli Institute of Nanoscience, Delft University of Technology, PO Box 5046, 2600 GA Delft, The Netherlands*

*Corresponding author: dohunkim@snu.ac.kr

Abstract

Silicon quantum dot spin qubits have become a promising platform for scalable quantum computing because of their small size and compatibility with industrial semiconductor manufacturing processes. Although Si/SiGe heterostructures are commonly used to host spin qubits due to their high mobility and low percolation density, the SiGe spacer creates a gap between the qubits and control electrodes, which limits the ability to tune exchange coupling. As a result, residual coupling leads to unwanted single-qubit phase shifts, making multi-qubit control more difficult. In this work, we explore swapping the roles of overlapping nanogates to overcome this issue. By reconfiguring the gate voltages, we demonstrate in situ role switching while maintaining multi-qubit control. Additionally, this method significantly improves the tunability of exchange coupling by several orders of magnitude over the traditional approach.

This strategy reduces unintended single-qubit phase shifts and minimizes the complexity of multi-qubit control, supporting scalable growth with minimal experimental overhead.

Keywords: quantum dot, electron spin qubits, quantum dot tuning, two-qubit interaction, Si/SiGe, coupling tunability

Spin qubits based on semiconductor quantum dots¹ have been extensively studied as a feasible technology for implementation in scalable quantum processors, largely motivated by their fabrication compatibility with industrial complementary metal-oxide-semiconductor (CMOS) technology.² Several studies have demonstrated the operation of one- and two-dimensional spin qubit arrays,³⁻⁷ high-fidelity single- and two-qubit gates,⁸⁻¹⁰ long-range coupling via a superconducting resonator,^{11,12} and operation at elevated temperatures, which significantly boosts the cooling power and offers advantages for quantum-classical chip integration.¹³⁻¹⁸ Building on this progress, high-fidelity initialization, readout, and manipulation of spin qubits have now been demonstrated within a single device, as validated by observing the violation of Bell's inequality.¹⁹ In parallel, the industrially mature CMOS fabrication technology has also motivated extensive research toward the high-throughput production of high-uniformity spin qubit devices.²⁰

The formation of quantum dots is a prerequisite for realizing spin qubits. This involves confining electrons or holes to specific regions by leveraging the properties of the material in combination with the electric potential generated by applying voltage to the nano-fabricated metal gates.²¹ In particular, silicon quantum dot qubits have been extensively studied, due to the high natural abundance of zero-nuclear-spin isotopes. Furthermore, residual nuclear spins can be further removed via isotopic enrichment to provide a magnetically quiet environment for the spin qubits.²² With this platform, the overlapping metal gate architecture has been widely adopted to realize tight electron confinement.^{4,8,9,23} In early device implementations, approaching the single-electron regime was a crucial objective, which prompted the fabrication of plunger gates with an appropriate width to ensure their energy controllability and sufficient coupling between quantum

dots. In many studies, a tuning strategy was employed in which quantum dots are formed beneath the plunger gates located below the barrier gate layer, a configuration referred to as *conventional tuning* in this work. Studies using this configuration have demonstrated that static tunnel coupling between quantum dots can be well controlled. However, as research efforts have increasingly shifted toward high-fidelity multi-qubit control, which often requires dynamic control of the coupling via barrier pulses,²⁴ the controllability achievable with barrier gates has proven limited, thereby motivating researchers to seek alternative approaches such as exploiting always-on exchange coupling.⁹ Meanwhile, spin shuttling, a potential pathway toward long-range coupling, has also been extensively studied in devices where plunger and barrier nanogates of nearly equal width are used to form and move quantum dots continuously.²⁵

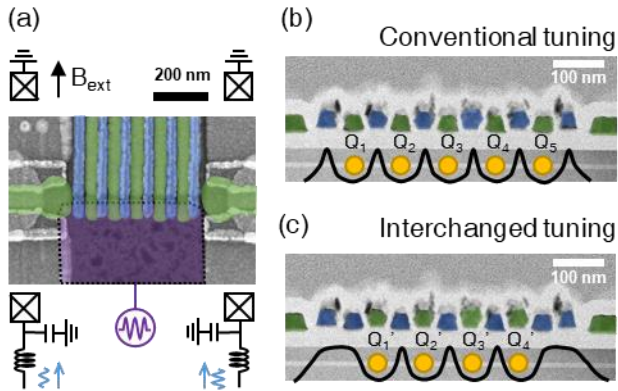


Figure 1.

In line with these efforts, we fabricated a quantum-dot qubit device with equal-width nanogates and investigated the effect of changing the tuning strategy. This approach, referred to as *interchanged tuning* hereafter, assigns the nanogates closer to (farther from) the spin qubits as barrier (plunger) gates. Using this tuning method, the well-defined formation of quantum dot single-spin qubits is demonstrated. Although previous studies on shuttling have shown that potential wells can be dynamically formed beneath each gate and moved continuously,²⁵ shifting multiple wells and energy barriers with maintained multi-qubit controllability has not been demonstrated in a similar gate structure. Here, we show that both of these are feasible with the proposed tuning strategy. Furthermore, the tunability of the exchange coupling is enhanced by several orders of magnitude for all nearest-neighbor pairs with a maximum value of 16.6 dec/V, while the controllability of the spin qubits is simultaneously maintained. We further discuss how this enhancement may influence future spin qubit experiments.

The device was fabricated on an isotopically enriched $^{28}\text{Si}/\text{SiGe}$ heterostructure wafer.²² First, a 20-nm-thick Al_2O_3 layer was deposited by atomic layer deposition (ALD) to serve as insulation, followed by three layers of Ti/Pd metallic gates and oxide layers using E-beam

lithography, E-beam evaporation, and ALD. The first of these layers consists of screening gates, which prevent the electric field from accessing the upper metal layers and locally deplete the two-dimensional electron gas (2DEG), thereby roughly defining a one-dimensional channel for quantum dot formation. The second and third layers are used to control either the energy of the quantum dots or the tunnel coupling between them. A micromagnet was fabricated on top of the metal layers to introduce a magnetic field gradient to enable individual qubits to be addressed and to enhance the controllability of spin qubits via electric dipole spin resonance (EDSR). The micromagnet was magnetized by applying an external in-plane magnetic field of 0.44 T in the direction as indicated in Figure 1a. The spin-qubit resonance frequency is typically in the range of 15–16 GHz. Single-qubit operation is achieved by applying microwave signals to the screening gate at the qubit frequency, which causes the spin qubit to experience an oscillating transverse magnetic field.²⁶ High-bandwidth spin qubit measurements were conducted by employing RF-reflectometry to apply a carrier signal to the ohmic contacts, which are connected to LC tank circuits composed of a commercial inductor and parasitic capacitance.²⁷ All gates were connected to DC voltage sources and to either an arbitrary waveform generator or a signal generator through on-board bias tees. The device was cooled in a dilution refrigerator, and the electron temperature was approximately 75 mK. Additional details of the experimental setup are provided in the Supporting Information (S1).

Figure 1b shows the gate configuration for the conventional tuning method, where the green (blue) gates located closer to (farther from) the 2DEG act as plunger (barrier) gates. The combination provides a potential energy landscape for an experiment using five quantum dots (Q_1, Q_2, Q_3, Q_4, Q_5) and two sensing dots for charge sensing, one on each side. Alternatively, the

roles of the nanogates can be switched by assigning the role of barrier gates to the gates closer to the 2DEG (Figure 1c). This approach allows the formation of four quantum dots (Q_1' , Q_2' , Q_3' , Q_4') with the given gate structure.

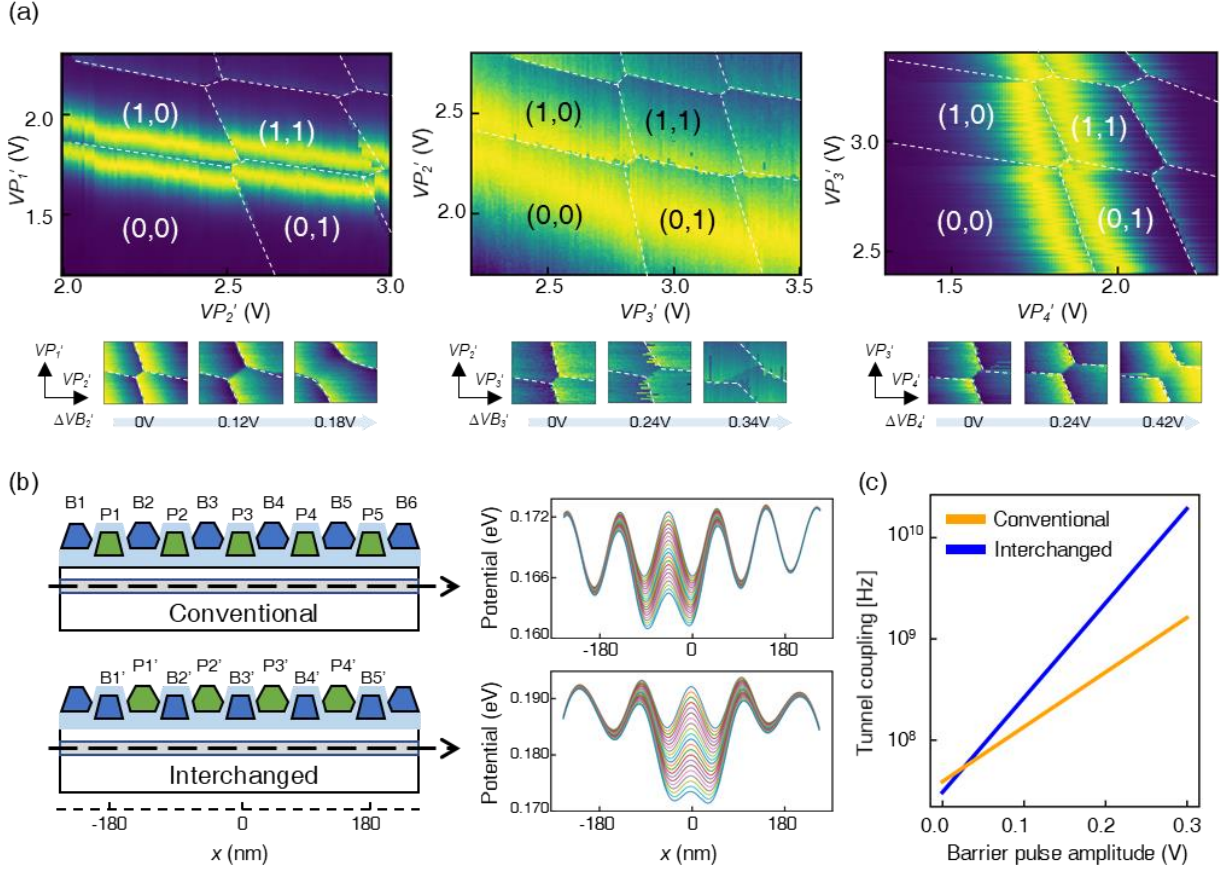


Figure 2.

First, the interchanged tuning method is shown to enable the single-electron regime to be reached for all quantum dots suitable for multi-qubit operation. Figure 2a shows the charge stability diagram for the few-electron regime of Q_1' - Q_2' , Q_2' - Q_3' , and Q_3' - Q_4' . Although the lever-arm of the newly mapped plungers is reduced, more than three-electron filling is achieved owing

to a high-quality 8-nm-thick intergate oxide layer, which prevents breakdown even under a few volts of potential difference between the gates. Parity readout was adopted using the Pauli spin blockade (PSB)^{28,29} for spin-state readout, a recent and widely used approach due to its deterministic readout time, applicability to isolated quantum dot qubits, and robust operation at elevated temperatures.^{13,30,31} By setting the charge occupation to (3,1,1,3), a wide PSB readout window was realized by exploiting orbital energy spacing rather than valley splitting.⁴ The expression (k,l,m,n) denotes the number of electrons in each quantum dot. Under this configuration, the newly designated barrier gates were observed to have the potential to vary the tunnel coupling between dots over a wide range, as qualitatively illustrated in the bottom insets to Fig. 2a. Compared with the conventional tuning method, the outermost quantum dots are farther from the sensor dots. Therefore, we used an integration time of 2 μ s, which is slightly longer than that of the conventional strategy, to maintain high-fidelity readout. Interchanged tuning produced a signal-to-noise ratio up to 10.6, which corresponds to a charge readout fidelity above 99.9%.³² (see Supporting Information S2)

The potential profile on 2DEG for the tuning strategies was simulated using COMSOL MULTIPHYSICS (Figure 2b). For both tuning methods, we calculated the potential profiles by varying the voltage applied to one of the additional barrier gates to a maximum of 0.3 V, considering the typical voltage range used in the experiment. As the barrier gate voltage of $B_3(B_3')$ increases, the potential barrier between $Q_2(Q_2')$ and $Q_3(Q_3')$ gradually decreases, which leads to stronger tunnel coupling. The change is more pronounced in the interchanged gate configuration than in the conventional one. Based on the simulation result, the tunnel coupling was calculated as a function of the barrier gate voltage by solving the single-particle Hamiltonian

between the quantum dots. As is evident from Figure 2c, the change in tunnel coupling exhibits a steeper gradient in the case of the interchanged tuning strategy.

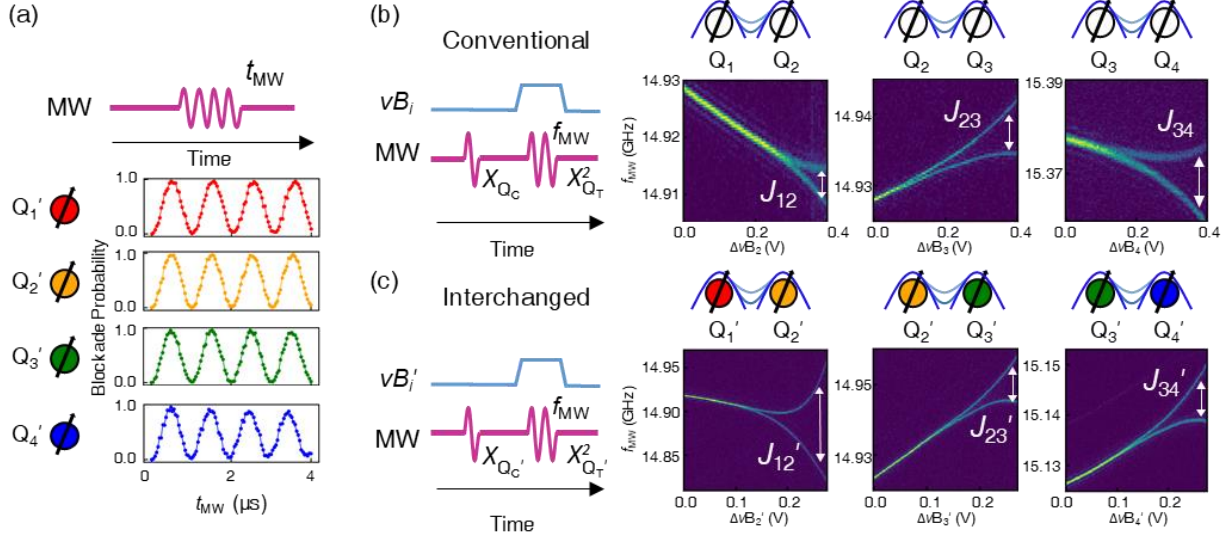


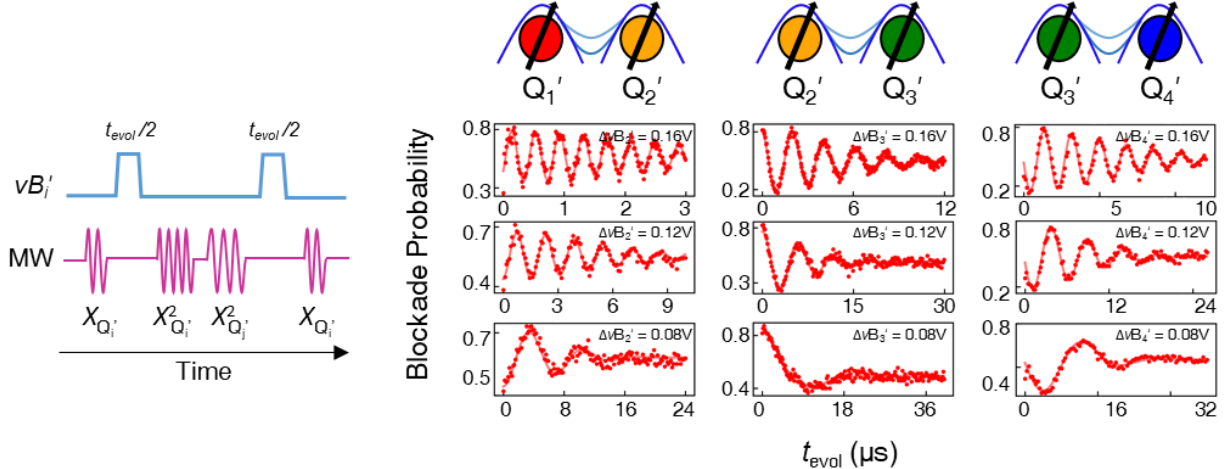
Figure 3.

Subsequently, we attempted to experimentally determine how the enhanced tunability of tunnel coupling, as revealed by simulation, translates into the tunability of exchange coupling. The spin qubits were manipulated at the symmetric point in the charge stability diagram, where the first derivative of the exchange coupling (J) with respect to detuning (Δ) vanishes (i.e., $\partial J / \partial \Delta = 0$).²⁴ Figure 3a shows that high-quality single-qubit control and addressing can be demonstrated under the interchanged tuning strategy. During the experiments, two pairs of qubits were initialized to odd-parity by adiabatically changing the detuning to move the single electron from the doubly-occupied singlet state to the other quantum dot⁴ (see Supporting Information S2). Variation of the burst duration (t_{MW}) of the microwave signal applied to the screening gate enabled the high-quality oscillations in the blockade probability to be observed. Although the

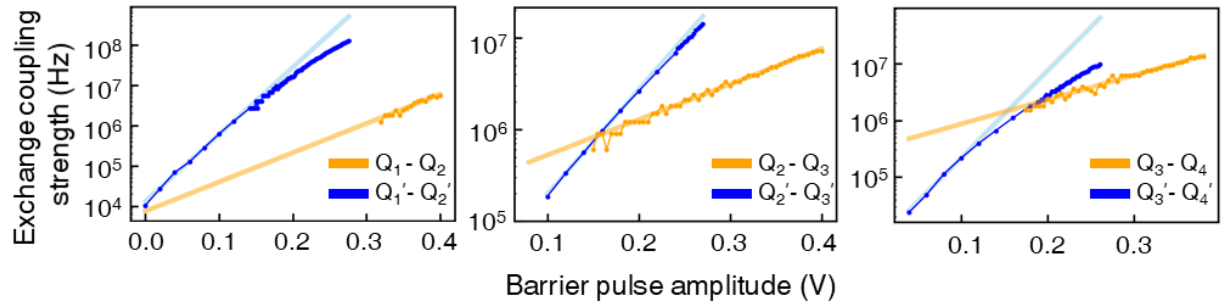
Rabi oscillation quality of Q_4' was limited, this was attributed to strong coupling with a nearby reservoir.³³

Exchange spectroscopy was used to quantify the achievable exchange coupling strength. The pulse sequence is illustrated in Figure 3b,c (left). First, the control qubit was rotated by $\pi/2$ about the x-axis. Then, a virtual barrier pulse (vB_i and vB_i') was applied to the gates between the qubits to increase their exchange coupling, and the microwave frequency (f_{MW}) was swept to determine the dependence of the resonance frequency on the exchange coupling. Figure 3b and 3c show the trend in exchange coupling, defined as the frequency difference between the two branches in a given exchange spectroscopy map, for the conventional and interchanged gate configurations, respectively. The global slope of the branches with respect to the barrier pulse amplitude arises from the spatial gradient of B_z generated by the micromagnet. For conventional tuning, the exchange coupling increased to only about 10 MHz with a 0.4 V barrier pulse. In contrast, the interchanged strategy could significantly enhance the coupling; for example, J_{12}' reached about 100 MHz at a 0.28 V barrier pulse for Q_1' - Q_2' . Although the degree of tunability varied among different qubit pairs, the tunability was clearly enhanced overall.

(a)



(b)

**Figure 4.**

The tunability of the exchange coupling strength was quantified more precisely by measuring the decoupled controlled-Z (dCZ) oscillation.³⁴ Evaluation of the tunability makes it necessary to examine a coupling strength smaller than the resonance linewidth. Considering that the initial condition without the barrier pulse may already have a relatively large J , the time-domain dCZ oscillations were used to verify the coupling behavior. In the pulse sequence in Figure 4a (left), intervening π -pulses (X^2) applied to both qubits cancel out the unwanted single-qubit phase accumulation, thus allowing us to observe the phase oscillations by J .³⁴ As shown in

Figure 4a (main panel), the data can be fitted to a decaying sinusoidal function to extract the frequency, which corresponds to $J/2$. Figure 4b compares the exchange coupling tunability between the two tuning methods based on the measured results. With the alternative tuning strategy, the dependence of the coupling strength on the barrier pulse amplitude is noticeably steeper. The data were fit to an exponential form by focusing on the few-MHz range typically used in experiments. The fitted tunability values are 7.25, 3.87, and 4.32 dec/V (16.6, 11.4, 15.4 dec/V) for the conventional (interchanged) gate configuration. Using the alternative tuning method, the tunability increases by several orders of magnitude for all-nearest-neighbor pairs, significantly exceeding that in the conventional case. Interestingly, the trend of exchange coupling does not follow a single-exponential form over the entire data range. A previous study showed that tunnel coupling asymptotically approaches a constant as the two quantum dots merge into a single larger quantum dot because the potential barrier is lowered by the barrier pulse.³⁵ This result is itself a consequence of the enhanced tunability of the coupling. This high tunability allows us to explore the entire coupling regime and, henceforth, is expected to help accurately calibrate the actual profile of exchange coupling as a function of the barrier-pulse amplitude.

The most plausible explanation for the increased tunability is a difference in the lever arm. However, when comparing the lever arms for each tuning strategy, the ratios are 1.75, 3.18, and 2.71, whereas the measured ratios for coupling controllability are 2.29, 2.95, and 3.56, respectively, for the case shown in Figure 4b. These results show that the enhancement cannot be explained solely by the lever-arm effect; in fact, it may originate from the uncertainty in the positions of the formed quantum dots and differences in the geometries of the two gate layers. As

shown above, this tuning strategy still allows us to construct virtual gates and suppress crosstalk, thereby enabling reliable multi-qubit control. These results demonstrate that the enhanced tunability can be maintained without introducing crosstalk that is sufficiently large to hinder qubit operation.

Residual exchange coupling induces unwanted ZZ operation, which complicates the resulting Hamiltonian. When a microwave signal is used to manipulate one of the qubits in a two-qubit system with residual coupling, the resulting time-evolution operator includes not only the single-qubit operation term but also contains an additional term proportional to $\frac{J}{\Omega}ZZ$.³⁶ Here, Ω denotes the Rabi frequency. This residual coupling limits the achievable single-qubit fidelity. Mitigation of this effect requires the coupling to be much smaller than the Rabi frequency ($J \ll \Omega$) as a fundamental requirement to achieve high single-qubit gate fidelity. However, to realize both single- and two-qubit operations with high fidelity, the coupling must be dynamically controlled on a short timescale, which is typically challenging to achieve with insufficient tunability. Even though a calibration routine could compensate for the undesired phase accumulation,⁸ this becomes increasingly challenging as the scale of the qubit system grows. Therefore, achieving exchange interaction such that it has sufficient tunability is crucial, and requires not only careful design of the gate geometry but also an optimal gate configuration for the experiment. From this perspective, the suggested tuning strategy provides a practical and efficient means to enhance the tunability of the exchange coupling simply by changing the voltage configuration within the same qubit device, without requiring any modification to the experimental setup.

In conclusion, we investigated the effectiveness of an alternative quantum dot tuning method, in which the roles of the nanogates that define the quantum dots are interchanged. Using the proposed strategy, we demonstrated the formation of quantum dots and single-qubit operation. Notably, the tunability of exchange coupling is enhanced by several orders of magnitude across all nearest-neighbor qubit pairs. The result is significant because it demonstrates the realization of tunability of approximately 16 dec/V in Si/SiGe devices, which has hitherto only been achieved in Si-MOS devices with a larger lever-arm.³⁷ Conventionally, the spin qubits in Si/SiGe devices are located far from the electrically noisy semiconductor-dielectric interface;²² however, the inherent distance between the qubits and metal electrodes limits the tunability of the coupling. By contrast, the proposed interchanged tuning strategy allows us to effectively exploit the advantages of the Si/SiGe platform, particularly for devices with limited interaction tunability. In addition, this method enables the formation of quantum dots beneath arbitrary gates. This flexibility allows the device properties to be studied more intensively by varying the location of the quantum dot used as a probe; for example, the magnetic gradient field to optimize micromagnet design, valley splitting as a function of position, and the spatial characteristics of noise originating from impurities and sensor dots. Further studies on fabrication strategies, including thinner gate oxides and advanced gate geometries, would contribute to bolstering the advantages of this strategy. This approach may provide a way to achieve sufficient coupling tunability with modest experimental effort, thereby facilitating convenient multi-qubit control, for example, by optimizing the PSB readout,³⁸ increasing the efficiency of the resonant SWAP gate operation,³⁹ and accurately engineering the Hamiltonian for Si/SiGe quantum dot spin qubit processors defined by the gate overlay.

Acknowledgments

This work was supported by a National Research Foundation of Korea (NRF) grant funded by the Korean Government (Ministry of Science and ICT (MSIT)) (RS-2023-00283291), RS-2024-00413957, SRC Center for Quantum Coherence in Condensed Matter RS-2023-00207732, RS-2023-NR077112 and Quantum Technology R&D Leading Program (Quantum Computing) RS-2024-00442994) and a core center program grant funded by the Ministry of Education (No. 2021R1A6C101B418). Lucas E. A. Stehouwer and Davide Degli Esposti developed and characterized the heterostructure under the supervision of Giordano Scappucci. Correspondence and requests for materials should be addressed to DK (dohunkim@snu.ac.kr).

Figure captions

Figure 1. $^{28}\text{Si}/\text{SiGe}$ linear quantum dot qubit device and schematic representation of tuning strategies

(a) Scanning electron microscopy image of the device. The squares with X symbols denote an ohmic contact through which a radio-frequency (RF) signal is injected via a tank circuit for RF reflectometry. The purple gate enclosed within the dashed line represents the screening gate, to which microwaves are applied for single-qubit manipulation. The gates colored green (blue) correspond to the second (third) metal layer. The micromagnet that was fabricated on top of the gates is omitted here for clarity.

(b-c) Transmission electron microscopy image showing a cross-section of a similar device fabricated in the same batch. The estimated electrostatic potential landscape and quantum dot locations for both tuning strategies are shown. For each strategy, the plunger and barrier gates are colored green and blue, respectively.

Figure 2. Charge stability diagram of double quantum dot pairs and coupling simulation

(a) Charge stability diagram of pairs of double-quantum dots. VP_i' denotes the voltage on the plunger gates P_i' in the interchanged configuration. Insets: changes as the voltage applied to the barrier gates becomes increasingly positive, with the text in each inset indicating the voltage increments. For $Q_2'-Q_3'$, the tunneling rate to the reservoir is slow compared with the time scale of voltage rastering, so that the transition lines appear latched.

- (b)** Simulated electric potential for the conventional and interchanged gate configurations. Left: device cross-section for the two tuning strategies. Right: corresponding simulated potential profile at the qubit location as the additional voltage on B3 and B3' is varied from 0 V to 0.3 V
- (c)** Tunnel coupling calculated from the simulated data for both tuning strategies.

Figure 3. Single-qubit controllability and exchange coupling spectroscopy

- (a)** Rabi oscillations of four qubits and the pulse sequence in the interchanged tuning method.
- (b-c)** Exchange spectroscopy with conventional tuning and interchanged tuning. vB_i and vB_i' denote the i-th virtual barrier gate voltage, while f_{MW} corresponds to the microwave frequencies applied to the target qubit. X (X^2) denotes a $\pi/2$ (π) rotation about the x -axis.

Figure 4. Enhanced tunability of exchange coupling

- (a)** Decoupled Controlled-Z oscillations of the qubits by applying a varying pulse amplitude to the barrier gates.
- (b)** Exchange coupling as a function of the barrier pulse amplitude. The blue (orange) trace shows data from an interchanged (conventional) gate configuration. The extracted tunabilities are 16.6 dec/V, 11.4 dec/V, and 15.4 dec/V (7.25 dec/V, 3.87 dec/V, and 4.32 dec/V) for the interchanged (conventional) gate configuration, obtained by fitting to $J = Ae^{Bv}$.

References

- (1) Loss, D.; DiVincenzo, D. P. Quantum Computation with Quantum Dots. *Phys. Rev. A* **1998**, *57* (1), 120–126. <https://doi.org/10.1103/PhysRevA.57.120>.
- (2) Maurand, R.; Jehl, X.; Kotekar-Patil, D.; Corna, A.; Bohuslavskyi, H.; Laviéville, R.; Hutin, L.; Barraud, S.; Vinet, M.; Sanquer, M.; De Franceschi, S. A CMOS Silicon Spin Qubit. *Nat. Commun.* **2016**, *7* (1), 13575. <https://doi.org/10.1038/ncomms13575>.
- (3) Takeda, K.; Noiri, A.; Nakajima, T.; Yoneda, J.; Kobayashi, T.; Tarucha, S. Quantum Tomography of an Entangled Three-Qubit State in Silicon. *Nat. Nanotechnol.* **2021**, *16* (9), 965–969. <https://doi.org/10.1038/s41565-021-00925-0>.
- (4) Philips, S. G. J.; Mądzik, M. T.; Amitonov, S. V.; de Snoo, S. L.; Russ, M.; Kalhor, N.; Volk, C.; Lawrie, W. I. L.; Brousse, D.; Tryputen, L.; Wuetz, B. P.; Sammak, A.; Veldhorst, M.; Scappucci, G.; Vandersypen, L. M. K. Universal Control of a Six-Qubit Quantum Processor in Silicon. *Nature* **2022**, *609* (7929), 919–924. <https://doi.org/10.1038/s41586-022-05117-x>.
- (5) Hendrickx, N. W.; Lawrie, W. I. L.; Russ, M.; van Riggelen, F.; de Snoo, S. L.; Schouten, R. N.; Sammak, A.; Scappucci, G.; Veldhorst, M. A Four-Qubit Germanium Quantum Processor. *Nature* **2021**, *591* (7851), 580–585. <https://doi.org/10.1038/s41586-021-03332-6>.
- (6) Zhang, X.; Morozova, E.; Rimbach-Russ, M.; Jirovec, D.; Hsiao, T.-K.; Fariña, P. C.; Wang, C.-A.; Oosterhout, S. D.; Sammak, A.; Scappucci, G.; Veldhorst, M.; Vandersypen, L. M. K. Universal Control of Four Singlet–Triplet Qubits. *Nat. Nanotechnol.* **2025**, *20* (2), 209–215. <https://doi.org/10.1038/s41565-024-01817-9>.
- (7) Unseld, F. K.; Undseth, B.; Raymenants, E.; Matsumoto, Y.; de Snoo, S. L.; Karwal, S.; Pietx-Casas, O.; Ivlev, A. S.; Meyer, M.; Sammak, A.; Veldhorst, M.; Scappucci, G.; Vandersypen, L. M. K. Baseband Control of Single-Electron Silicon Spin Qubits in Two Dimensions. *Nat. Commun.* **2025**, *16* (1), 5605. <https://doi.org/10.1038/s41467-025-60351-x>.
- (8) Xue, X.; Russ, M.; Samkharadze, N.; Undseth, B.; Sammak, A.; Scappucci, G.; Vandersypen, L. M. K. Quantum Logic with Spin Qubits Crossing the Surface Code Threshold. *Nature* **2022**, *601* (7893), 343–347. <https://doi.org/10.1038/s41586-021-04273-w>.
- (9) Noiri, A.; Takeda, K.; Nakajima, T.; Kobayashi, T.; Sammak, A.; Scappucci, G.; Tarucha, S. Fast Universal Quantum Gate above the Fault-Tolerance Threshold in Silicon. *Nature* **2022**, *601* (7893), 338–342. <https://doi.org/10.1038/s41586-021-04182-y>.
- (10) Mills, A. R.; Guinn, C. R.; Gullans, M. J.; Sigillito, A. J.; Feldman, M. M.; Nielsen, E.; Petta, J. R. Two-Qubit Silicon Quantum Processor with Operation Fidelity Exceeding 99%. *Sci. Adv.* **2022**, *8* (14), eabn5130. <https://doi.org/10.1126/sciadv.abn5130>.
- (11) Samkharadze, N.; Zheng, G.; Kalhor, N.; Brousse, D.; Sammak, A.; Mendes, U. C.; Blais, A.; Scappucci, G.; Vandersypen, L. M. K. Strong Spin-Photon Coupling in Silicon. *Science* **2018**, *359* (6380), 1123–1127. <https://doi.org/10.1126/science.aar4054>.
- (12) Dijkema, J.; Xue, X.; Harvey-Collard, P.; Rimbach-Russ, M.; de Snoo, S. L.; Zheng, G.; Sammak, A.; Scappucci, G.; Vandersypen, L. M. K. Cavity-Mediated iSWAP Oscillations between Distant Spins. *Nat. Phys.* **2025**, *21* (1), 168–174. <https://doi.org/10.1038/s41567-024-02694-8>.

- (13) Yang, C. H.; Leon, R. C. C.; Hwang, J. C. C.; Saraiva, A.; Tanttu, T.; Huang, W.; Camirand Lemyre, J.; Chan, K. W.; Tan, K. Y.; Hudson, F. E.; Itoh, K. M.; Morello, A.; Pioro-Ladrière, M.; Laucht, A.; Dzurak, A. S. Operation of a Silicon Quantum Processor Unit Cell above One Kelvin. *Nature* **2020**, *580* (7803), 350–354. <https://doi.org/10.1038/s41586-020-2171-6>.
- (14) Petit, L.; Eenink, H. G. J.; Russ, M.; Lawrie, W. I. L.; Hendrickx, N. W.; Philips, S. G. J.; Clarke, J. S.; Vandersypen, L. M. K.; Veldhorst, M. Universal Quantum Logic in Hot Silicon Qubits. *Nature* **2020**, *580* (7803), 355–359. <https://doi.org/10.1038/s41586-020-2170-7>.
- (15) Camenzind, L. C.; Geyer, S.; Fuhrer, A.; Warburton, R. J.; Zumbühl, D. M.; Kuhlmann, A. V. A Hole Spin Qubit in a Fin Field-Effect Transistor above 4 Kelvin. *Nat. Electron.* **2022**, *5* (3), 178–183. <https://doi.org/10.1038/s41928-022-00722-0>.
- (16) Huang, J. Y.; Su, R. Y.; Lim, W. H.; Feng, M.; van Straaten, B.; Severin, B.; Gilbert, W.; Dumoulin Stuyck, N.; Tanttu, T.; Serrano, S.; Cifuentes, J. D.; Hansen, I.; Seedhouse, A. E.; Vahapoglu, E.; Leon, R. C. C.; Abrosimov, N. V.; Pohl, H.-J.; Thewalt, M. L. W.; Hudson, F. E.; Escott, C. C.; Ares, N.; Bartlett, S. D.; Morello, A.; Saraiva, A.; Laucht, A.; Dzurak, A. S.; Yang, C. H. High-Fidelity Spin Qubit Operation and Algorithmic Initialization above 1 K. *Nature* **2024**, *627* (8005), 772–777. <https://doi.org/10.1038/s41586-024-07160-2>.
- (17) Xue, X.; Patra, B.; van Dijk, J. P. G.; Samkharadze, N.; Subramanian, S.; Corma, A.; Paquelet Wuetz, B.; Jeon, C.; Sheikh, F.; Juarez-Hernandez, E.; Esparza, B. P.; Rampurawala, H.; Carlton, B.; Ravikumar, S.; Nieva, C.; Kim, S.; Lee, H.-J.; Sammak, A.; Scappucci, G.; Veldhorst, M.; Sebastian, F.; Babaie, M.; Pellerano, S.; Charbon, E.; Vandersypen, L. M. K. CMOS-Based Cryogenic Control of Silicon Quantum Circuits. *Nature* **2021**, *593* (7858), 205–210. <https://doi.org/10.1038/s41586-021-03469-4>.
- (18) Bartee, S. K.; Gilbert, W.; Zuo, K.; Das, K.; Tanttu, T.; Yang, C. H.; Dumoulin Stuyck, N.; Pauka, S. J.; Su, R. Y.; Lim, W. H.; Serrano, S.; Escott, C. C.; Hudson, F. E.; Itoh, K. M.; Laucht, A.; Dzurak, A. S.; Reilly, D. J. Spin-Qubit Control with a Milli-Kelvin CMOS Chip. *Nature* **2025**, *643* (8071), 382–387. <https://doi.org/10.1038/s41586-025-09157-x>.
- (19) Steinacker, P.; Tanttu, T.; Lim, W. H.; Dumoulin Stuyck, N.; Feng, M.; Serrano, S.; Vahapoglu, E.; Su, R. Y.; Huang, J. Y.; Jones, C.; Itoh, K. M.; Hudson, F. E.; Escott, C. C.; Morello, A.; Saraiva, A.; Yang, C. H.; Dzurak, A. S.; Laucht, A. Bell Inequality Violation in Gate-Defined Quantum Dots. *Nat. Commun.* **2025**, *16* (1), 3606. <https://doi.org/10.1038/s41467-025-57987-0>.
- (20) Neyens, S.; Zietz, O. K.; Watson, T. F.; Luthi, F.; Nethewewala, A.; George, H. C.; Henry, E.; Islam, M.; Wagner, A. J.; Borjans, F.; Connors, E. J.; Corrigan, J.; Curry, M. J.; Keith, D.; Kotlyar, R.; Lampert, L. F.; Mądzik, M. T.; Millard, K.; Mohiyaddin, F. A.; Pellerano, S.; Pillarisetty, R.; Ramsey, M.; Savytskyy, R.; Schaal, S.; Zheng, G.; Ziegler, J.; Bishop, N. C.; Bojarski, S.; Roberts, J.; Clarke, J. S. Probing Single Electrons across 300-Mm Spin Qubit Wafers. *Nature* **2024**, *629* (8010), 80–85. <https://doi.org/10.1038/s41586-024-07275-6>.
- (21) Hanson, R.; Kouwenhoven, L. P.; Petta, J. R.; Tarucha, S.; Vandersypen, L. M. K. Spins in Few-Electron Quantum Dots. *Rev. Mod. Phys.* **2007**, *79* (4), 1217–1265. <https://doi.org/10.1103/RevModPhys.79.1217>.
- (22) Degli Esposti, D.; Paquelet Wuetz, B.; Fezzi, V.; Lodari, M.; Sammak, A.; Scappucci, G. Wafer-Scale Low-Disorder 2DEG in 28Si/SiGe without an Epitaxial Si Cap. *Appl. Phys.*

- Lett.* **2022**, *120* (18), 184003. <https://doi.org/10.1063/5.0088576>.
- (23) Zajac, D. M.; Hazard, T. M.; Mi, X.; Wang, K.; Petta, J. R. A Reconfigurable Gate Architecture for Si/SiGe Quantum Dots. *Appl. Phys. Lett.* **2015**, *106* (22), 223507. <https://doi.org/10.1063/1.4922249>.
- (24) Reed, M. D.; Maune, B. M.; Andrews, R. W.; Borselli, M. G.; Eng, K.; Jura, M. P.; Kiselev, A. A.; Ladd, T. D.; Merkel, S. T.; Milosavljevic, I.; Pritchett, E. J.; Rakher, M. T.; Ross, R. S.; Schmitz, A. E.; Smith, A.; Wright, J. A.; Gyure, M. F.; Hunter, A. T. Reduced Sensitivity to Charge Noise in Semiconductor Spin Qubits via Symmetric Operation. *Phys. Rev. Lett.* **2016**, *116* (11), 110402. <https://doi.org/10.1103/PhysRevLett.116.110402>.
- (25) Seidler, I.; Struck, T.; Xue, R.; Focke, N.; Trellenkamp, S.; Bluhm, H.; Schreiber, L. R. Conveyor-Mode Single-Electron Shuttling in Si/SiGe for a Scalable Quantum Computing Architecture. *npj Quantum Inf.* **2022**, *8* (1), 100. <https://doi.org/10.1038/s41534-022-00615-2>.
- (26) Pioro-Ladrière, M.; Obata, T.; Tokura, Y.; Shin, Y.-S.; Kubo, T.; Yoshida, K.; Taniyama, T.; Tarucha, S. Electrically Driven Single-Electron Spin Resonance in a Slanting Zeeman Field. *Nat. Phys.* **2008**, *4* (10), 776–779. <https://doi.org/10.1038/nphys1053>.
- (27) Liu, Y.-Y.; Philips, S. G. J.; Orona, L. A.; Samkharadze, N.; McJunkin, T.; MacQuarrie, E. R.; Eriksson, M. A.; Vandersypen, L. M. K.; Yacoby, A. Radio-Frequency Reflectometry in Silicon-Based Quantum Dots. *Phys. Rev. Appl.* **2021**, *16* (1), 014057. <https://doi.org/10.1103/PhysRevApplied.16.014057>.
- (28) Engel, H.-A.; Loss, D. Fermionic Bell-State Analyzer for Spin Qubits. *Science* **2005**, *309* (5734), 586–588. <https://doi.org/10.1126/science.1113203>.
- (29) Seedhouse, A. E.; Tanttu, T.; Leon, R. C. C.; Zhao, R.; Tan, K. Y.; Hensen, B.; Hudson, F. E.; Itoh, K. M.; Yoneda, J.; Yang, C. H.; Morello, A.; Laucht, A.; Coppersmith, S. N.; Saraiva, A.; Dzurak, A. S. Pauli Blockade in Silicon Quantum Dots with Spin-Orbit Control. *PRX Quantum* **2021**, *2* (1), 010303. <https://doi.org/10.1103/PRXQuantum.2.010303>.
- (30) Camenzind, L. C.; Geyer, S.; Fuhrer, A.; Warburton, R. J.; Zumbühl, D. M.; Kuhlmann, A. V. A Hole Spin Qubit in a Fin Field-Effect Transistor above 4 Kelvin. *Nat. Electron.* **2022**, *5* (3), 178–183. <https://doi.org/10.1038/s41928-022-00722-0>.
- (31) Niegemann, D. J.; El-Homsy, V.; Jadot, B.; Nurizzo, M.; Cardoso-Paz, B.; Chanrion, E.; Dartailh, M.; Klemt, B.; Thiney, V.; Bäuerle, C.; Mortemousque, P.-A.; Bertrand, B.; Niebojewski, H.; Vinet, M.; Balestro, F.; Meunier, T.; Urdampilleta, M. Parity and Singlet-Triplet High-Fidelity Readout in a Silicon Double Quantum Dot at 0.5 K. *PRX Quantum* **2022**, *3* (4), 040335. <https://doi.org/10.1103/PRXQuantum.3.040335>.
- (32) Serrano, S. Improved Single-Shot Qubit Readout Using Twin Rf-SET Charge Correlations. *PRX Quantum* **2024**, *5* (1). <https://doi.org/10.1103/PRXQuantum.5.010301>.
- (33) Veldhorst, M.; Yang, C. H.; Hwang, J. C. C.; Huang, W.; Dehollain, J. P.; Muhonen, J. T.; Simmons, S.; Laucht, A.; Hudson, F. E.; Itoh, K. M.; Morello, A.; Dzurak, A. S. A Two-Qubit Logic Gate in Silicon. *Nature* **2015**, *526* (7573), 410–414. <https://doi.org/10.1038/nature15263>.
- (34) Watson, T. F.; Philips, S. G. J.; Kawakami, E.; Ward, D. R.; Scarlino, P.; Veldhorst, M.; Savage, D. E.; Lagally, M. G.; Friesen, M.; Coppersmith, S. N.; Eriksson, M. A.; Vandersypen, L. M. K. A Programmable Two-Qubit Quantum Processor in Silicon. *Nature*

- 2018, 555 (7698), 633–637. <https://doi.org/10.1038/nature25766>.
- (35) Li, Q.; Cywiński, Ł.; Culcer, D.; Hu, X.; Das Sarma, S. Exchange Coupling in Silicon Quantum Dots: Theoretical Considerations for Quantum Computation. *Phys. Rev. B* **2010**, 81 (8), 085313. <https://doi.org/10.1103/PhysRevB.81.085313>.
 - (36) Heinz, I.; Mills, A. R.; Petta, J. R.; Burkard, G. Analysis and Mitigation of Residual Exchange Coupling in Linear Spin-Qubit Arrays. *Phys. Rev. Res.* **2024**, 6 (1), 013153. <https://doi.org/10.1103/PhysRevResearch.6.013153>.
 - (37) Tanttu, T.; Lim, W. H.; Huang, J. Y.; Dumoulin Stuyck, N.; Gilbert, W.; Su, R. Y.; Feng, M.; Cifuentes, J. D.; Seedhouse, A. E.; Seritan, S. K.; Ostrove, C. I.; Rudinger, K. M.; Leon, R. C. C.; Huang, W.; Escott, C. C.; Itoh, K. M.; Abrosimov, N. V.; Pohl, H.-J.; Thewalt, M. L. W.; Hudson, F. E.; Blume-Kohout, R.; Bartlett, S. D.; Morello, A.; Laucht, A.; Yang, C. H.; Saraiva, A.; Dzurak, A. S. Assessment of the Errors of High-Fidelity Two-Qubit Gates in Silicon Quantum Dots. *Nat. Phys.* **2024**, 20 (11), 1804–1809. <https://doi.org/10.1038/s41567-024-02614-w>.
 - (38) Takeda, K.; Noiri, A.; Nakajima, T.; Camenzind, L. C.; Kobayashi, T.; Sammak, A.; Scappucci, G.; Tarucha, S. Rapid Single-Shot Parity Spin Readout in a Silicon Double Quantum Dot with Fidelity Exceeding 99%. *npj Quantum Inf.* **2024**, 10 (1), 22. <https://doi.org/10.1038/s41534-024-00813-0>.
 - (39) Sigillito, A. J.; Gullans, M. J.; Edge, L. F.; Borselli, M.; Petta, J. R. Coherent Transfer of Quantum Information in a Silicon Double Quantum Dot Using Resonant SWAP Gates. *npj Quantum Inf.* **2019**, 5 (1), 110. <https://doi.org/10.1038/s41534-019-0225-0>.

Supporting Information

S1. Experimental setup

The quantum dot qubit device was mounted in a dilution refrigerator (Oxford Instruments Triton-500) with the mixing chamber plate kept at approximately 8 mK. All metal gates and ohmic contacts were connected to DC voltage sources (SIM928, Stanford Research Systems), with some additionally linked to either an arbitrary waveform generator (AWG, Quantum Machines OPX+) or a signal generator (Quantum Machines Octave) via on-board bias tees. The I/Q signals from the AWG were fed into the Octave, which functions as a local oscillator and up-converter, producing I/Q modulated microwave signals used to manipulate the spin qubits. Other baseband signals were employed to adjust the quantum dot energy levels or tunnel coupling abruptly. A lock-in amplifier (Zurich Instruments UHFLI) provided combined RF signals at the resonant frequencies of the two LC tank circuits, directed respectively to the two ohmic contacts. These RF signals, modulated by the conductance of the sensor dots, were reflected out and amplified by 45 dB through two series-connected cryogenic amplifiers (Cosmic Microwave Technology CITLF2), followed by an additional 25 dB of gain from a room-temperature amplifier (Lotus Communication Systems LNA100M2P0G). The amplified RF signals were then demodulated by a lock-in amplifier and digitized by the OPX+.

S2. Initialization and measurement process of the two tuning strategies

With the conventional tuning strategy, the charge occupation was set to (3,1,1,1,3). To implement the Pauli-spin-blockade-based parity readout, we reduced the interdot tunneling coupling until triplet-state latching was observed in the charge stability measurements. The signal-to-noise ratios (SNRs) of the left and right sensor dots were 13.9 and 6.54, respectively, as shown in Figure S1a. We carried out the initialization procedure illustrated in Figure S1b to ensure that the two pairs of qubits had odd parity and that Q3 was initialized in the spin-down state. During the “init1” process, if the measured parity was even, Q2 or Q4 in each pair was rotated by π . As shown in Figure S1c, we observed Rabi oscillations in all five qubits; however, the oscillations of Q3 and Q5 were not optimized. We attribute this to the imperfect initialization of Q3 and the strong coupling with the nearby reservoir.

For the interchanged tuning strategy, the outermost qubits were placed farther from the neighboring sensor dot than before. Still, the SNRs of the sensors on the left and right (7.48 and 4.97, respectively) with an integration time of 2 μ s remained sufficient to resolve the parity of the qubits (Figure S2a). Spin-qubit experiments used the initialization sequence shown in Figure S2b. The same “init1” process, where a conditional π -pulse was applied to Q2' or Q3', was used. An extra “init2” process employed a zCNOT gate on Q1' and Q4', based on controlled rotation, to reliably prepare the two-spin states. Then, we successfully initialized the $|0\rangle$ state, as shown by the results in Figure S2c, which features nearly a single resonance branch in the exchange spectroscopy measurement depending on the control qubit state. In each panel, the qubit symbols

indicate the control qubits, and each panel displays the resonances of Q2', Q3', and Q4' from left to right.

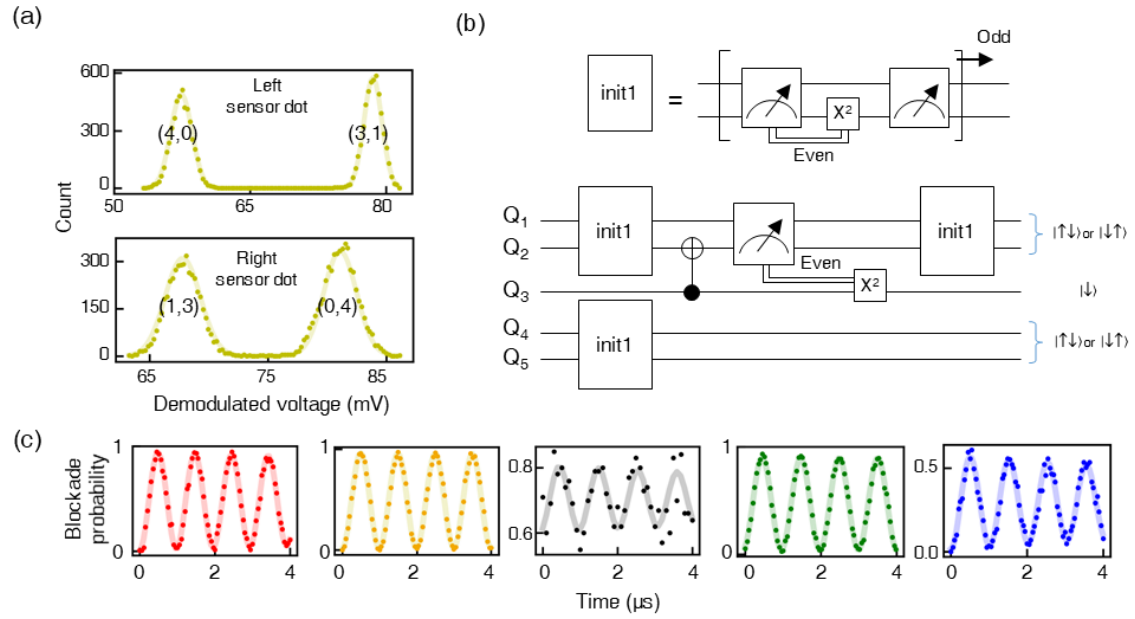


Figure S1. Initialization process and measurement using the conventional strategy

- (a) Histogram of the digitized sensor dot signal with the conventional tuning strategy.
- (b) Schematics of the initialization process for five-spin qubits.
- (c) Rabi oscillations of the five spin qubits.

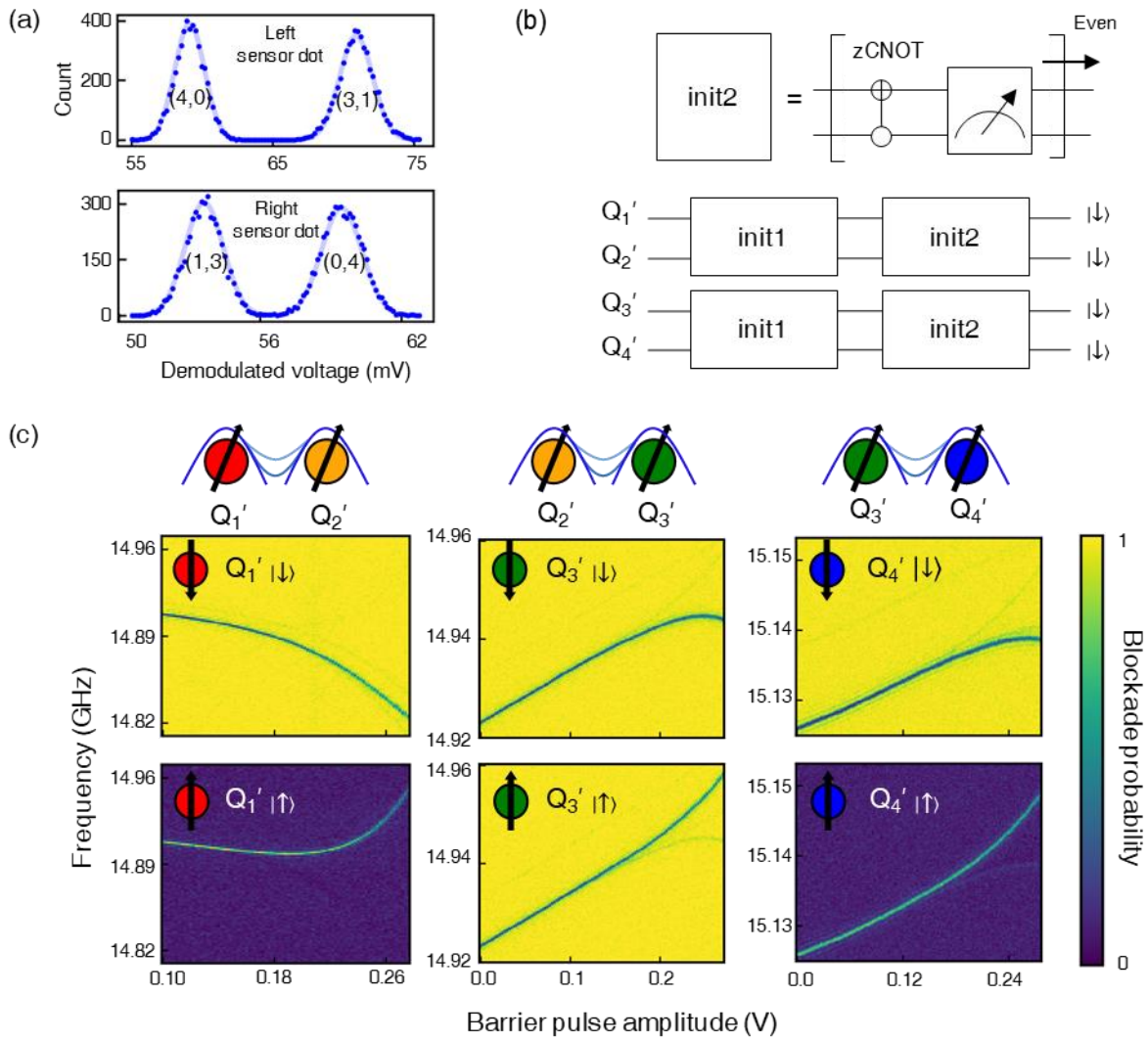


Figure S2. Initialization process and measurement with the interchanged tuning strategy

(a) Histogram of the digitized sensor dot signal.

(b) Schematics of the initialization process for four-spin qubits.

(c) Exchange spectroscopy measurements after the initialization process.

S3. Simulation of electric potential and tunnel coupling

The electrostatic confinement potential and tunnel coupling were simulated prior to experimental validation of the interchanged tuning strategy. The layer stack and individual layer thicknesses of the $^{28}\text{Si}/\text{SiGe}$ wafer adhered to the specifications reported in a previous study.² The morphology of the gate oxide layer (Al_2O_3 20 nm), metal gate layers (Ti 5 nm, Pd 30 nm), and intervening oxide layers (Al_2O_3 8 nm) were reflected in the simulation via observing a cross-sectional transmission electron microscope image of the device prepared in the same fabrication batch as the device used in the experiment. We employed COMSOL MULTIPHYSICS to generate an electric potential at the location of the two-dimensional electron gas (2DEG), which was estimated to reside at the interface between the ^{28}Si well and the SiGe barrier layer. After specifying the boundary conditions and gate voltages, we solved Poisson's equation self-consistently with the 2DEG charge density within the Thomas-Fermi approximation³

$$\rho_{2\text{DEG}}(V) = -e \frac{g_v m_t^*}{\pi \hbar^2} (E_F + eV) \Theta(E_F + eV) \quad (1)$$

Here, g_v denotes the valley degeneracy, m_t^* is the transverse electron effective mass, and $\Theta(x)$ is the Heaviside step function. In this simulation, we set $g_v = 2$ and $E_F = 0$. By varying the voltage levels applied to the barrier gate ($vB3$ and $vB3'$), we obtained the two-dimensional electrostatic potential maps and subsequently solved the single-particle Hamiltonian in a maximally localized basis to extract the off-diagonal tunnel-coupling term.

Supplementary references

- (1) Philips, S. G. J.; Mądzik, M. T.; Amitonov, S. V.; de Snoo, S. L.; Russ, M.; Kalhor, N.; Volk, C.; Lawrie, W. I. L.; Brousse, D.; Tryputen, L.; Wuetz, B. P.; Sammak, A.; Veldhorst, M.; Scappucci, G.; Vandersypen, L. M. K. Universal Control of a Six-Qubit Quantum Processor in Silicon. *Nature* **2022**, *609* (7929), 919–924. <https://doi.org/10.1038/s41586-022-05117-x>.
- (2) Degli Esposti, D.; Paquelet Wuetz, B.; Fezzi, V.; Lodari, M.; Sammak, A.; Scappucci, G. Wafer-Scale Low-Disorder 2DEG in 28Si/SiGe without an Epitaxial Si Cap. *Appl. Phys. Lett.* **2022**, *120* (18), 184003. <https://doi.org/10.1063/5.0088576>.
- (3) Schmidt, A. R.; Henry, E.; Lo, C. C.; Wang, Y.-T.; Li, H.; Greenman, L.; Namaan, O.; Schenkel, T.; Whaley, K. B.; Bokor, J.; Yablonovitch, E.; Siddiqi, I. A Prototype Silicon Double Quantum Dot with Dispersive Microwave Readout. *J. Appl. Phys.* **2014**, *116* (4). <https://doi.org/10.1063/1.4890835>.